

## EDGE ARTICLE

Cite this: *Chem. Sci.*, 2024, 15, 20303

All publication charges for this article have been paid for by the Royal Society of Chemistry

Tailoring hierarchical MnO<sub>2</sub> nanostructures on self-supporting cathodes for high-mass-loading zinc-ion batteries†Weijie Zheng,<sup>a</sup> Zhibiao Cui,<sup>a</sup> Cong Liu,<sup>c</sup> Libei Yuan,<sup>d</sup> Shengsong Li,<sup>a</sup> Lilin Lin,<sup>a</sup> Tao Meng,<sup>id</sup>\*<sup>a</sup> Liangui Yang,<sup>a</sup> Yexiang Tong,<sup>id</sup>\*<sup>c</sup> and Dong Shu,<sup>id</sup>\*<sup>ab</sup>

Aqueous zinc-ion batteries (AZIBs) with MnO<sub>2</sub> cathodes have promising application prospects; however, their performance is hindered by their low efficiency and insufficient life. By leveraging the nanomicellar properties of cetyltrimethylammonium bromide (CTAB), a hierarchical δ-MnO<sub>2</sub> with 2D/3D structure was directionally grown on a modified carbon cloth (CC) collector for realizing high-mass-loading AZIBs. Experimental results reveal the synergistic effects of micro/nano hierarchically structured MnO<sub>2</sub>–CC heterointerfaces in accelerating the electron migration and transfer rate of Zn<sup>2+</sup>/H<sup>+</sup>. Functioning as a conductive skeleton and flexible substrate, CC efficiently improves the reaction kinetics and buffers the interfacial stress resulting from the structural evolution of MnO<sub>2</sub> during the long-term electrode reaction. This phenomenon is investigated using advanced characterisation techniques, including X-ray absorption fine structure spectroscopy, Kelvin probe force microscopy, and theoretical simulations. The fabricated electrode exhibits superior electrochemical properties, such as high capacity (409.6 mA h g<sup>−1</sup> at 0.1 A g<sup>−1</sup>) and reliable cycling performance (with 86.6% capacity retention after 2000 cycles at 1.0 A g<sup>−1</sup>). Even at a high mass loading of 6.0 mg cm<sup>−2</sup>, the battery retains 81.8% of its original capacity after 1300 cycles. The proposed interface engineering strategy provides valuable insights into realising high-loading and long-life AZIBs.

Received 12th September 2024  
Accepted 10th November 2024

DOI: 10.1039/d4sc06182a

rsc.li/chemical-science

## 1 Introduction

High-performance electrochemical devices are crucial for achieving a carbon-neutral economy and energy transition.<sup>1–3</sup> Among all feasible options, aqueous zinc-ion batteries (AZIBs) have garnered wide attention due to their environmental friendliness, reliable safety, and high ionic conductivity.<sup>4,5</sup> To achieve high-performance AZIBs, an ideal cathode must be selected. To this end, several cathodes have been considered as promising since they reversibly intercalate/extract Zn<sup>2+</sup> during the discharging/charging process, such as V-based oxides, Mn-based oxides, and Prussian blue analogues.<sup>6,7</sup> Among them, transition metal oxides, especially manganese dioxide (MnO<sub>2</sub>),

have been extensively investigated because of their natural abundance, cost-effectiveness, high voltage platform and high theoretical capacity (Mn<sup>4+</sup>/Mn<sup>2+</sup>, 616 mA h g<sup>−1</sup>).<sup>8</sup> Although MnO<sub>2</sub> has various polymorphs (such as α-, β-, γ-, δ-, λ-, and ε-MnO<sub>2</sub>), it has been hindered by rapid capacity decay and short cycle life owing to the irreversible phase transformations, low electrical conductivity, and Jahn–Teller effect.<sup>9–11</sup>

Therefore, morphological design strategies have been employed to fabricate various MnO<sub>2</sub> structures such as 2D nanosheets, 3D nanocubes and nanoflowers.<sup>12,13</sup> Compared with blocks or shapeless materials, special structural morphologies considerably improve electrolyte wettability, enhance the surface area and increase the number of active sites for ion adsorption that are conducive to ion diffusion kinetics. For instance, Cai *et al.* designed MnO<sub>2</sub> nanocubes with a δ-MnO<sub>2</sub> nanolayer covering, which exhibited a stable capacity retention of 85.9% after 1000 cycles in AZIBs.<sup>14</sup> The δ-MnO<sub>2</sub> nanolayer acted as an interphase, thereby improving the H<sup>+</sup>/Zn<sup>2+</sup> kinetics and enhancing the electrochemical performance. The nanocube morphology, on the other hand, provided structural stability to withstand material deformation during ion shuttle reactions. Li *et al.* created flower-like δ-MnO<sub>2</sub> with abundant oxygen vacancies, which provided a large surface area for reversible phase transition *via* fast H<sup>+</sup>/Zn<sup>2+</sup> co-insertion.<sup>15</sup> The regular 3D morphology effectively mitigates structural

<sup>a</sup>School of Chemistry, South China Normal University, Guangzhou, 510006, People's Republic of China. E-mail: mengt@scnu.edu.cn; dshu@scnu.edu.cn

<sup>b</sup>National and Local Joint Engineering Research Center of MPES in High Energy and Safety LIBs, South China Normal University, Guangzhou, 510006, People's Republic of China

<sup>c</sup>MOE of the Key Laboratory of Bioinorganic and Synthetic Chemistry, The Key Lab of Low-Carbon Chemistry & Energy Conservation of Guangdong Province, School of Chemistry, Sun Yat-sen University, Guangzhou 510275, People's Republic of China

<sup>d</sup>Institute for Superconducting and Electronic Materials, Australian Institute for Innovative Materials, University of Wollongong, Wollongong, NSW, 2522, Australia

† Electronic supplementary information (ESI) available. See DOI: <https://doi.org/10.1039/d4sc06182a>



collapse during long-term cycling, and thus, the functional electrode demonstrated excellent retention of 83% after 1500 cycles. However, these studies fabricated electrodes using binder-assisted methods, in which inert polymer binders cause the local deactivation of active materials. This shielded area hinders ion and electron transfer, thereby degrading the overall performance of the electrode. The uninduced morphological growth easily leads to material stacking, and the active  $\text{MnO}_2$  tends to detach from the current collector under high-mass-loading conditions. Therefore, stack-free/free-standing  $\text{MnO}_2$  nanomaterials with a hierarchical structure must be grown on a stable substrate through a directional induction method, which is a key requirement for achieving high-loading, high-areal capacity electrodes.

By combining  $\text{MnO}_2$  with a conductive substrate, the conductivity and mass loading of electrodes can be improved.<sup>16</sup> Carbon cloth (CC) has emerged as a potential flexible conductive substrate for supporting active materials, providing a buffer against structural strains due to its deformable flexible interface. The inert carbon substrate provides a reliable growth base for attaching abundant active materials. For example, Zhang *et al.* developed a facile activation strategy to modify CC, and achieved excellent conductivity with a high specific capacity of  $580 \text{ mA h g}^{-1}$  at  $152 \text{ mA cm}^{-2}$  for use as the cathode for zinc–air batteries.<sup>17</sup> Zhao *et al.* designed an ultrafast method to synthesise NiCo layered double hydroxides on flexible CC (NiCo LDH@CC) as the cathode for aqueous alkaline Zn batteries, which exhibited superior flexibility and stability.<sup>18</sup> Although these studies have highlighted the effectiveness of CC in enhancing electron transport as a current collector for active materials, most have focused on modifying active materials, with limited surface-active sites and dispersed ion transport channels. Moreover, binding interaction between the active materials and the CC surface was ignored during the synthesis, which resulted in poor electrochemical performance due to loose contact. This oversight negatively impacts the transport efficiency of electrons in the electrode and hampers fast ion diffusion in high-mass-loading electrodes.

Herein, we design a micro/nano hierarchically structured  $\text{MnO}_2$  self-supporting CC (denoted as MNSMO@CC) electrode through a molecular manipulation strategy employing CTAB nanomicelles for AZIBs. This nanomicellar approach successfully facilitated strong interaction at the  $\text{MnO}_2$ –CC interface, forming an integrated structure. Moreover, the Jahn–Teller effect of  $\text{MnO}_2$  was effectively alleviated by the synergy of the hierarchical nanoarchitecture and CC. The MNSMO@CC cathode thus exhibited exceptional specific capacitance ( $409.6 \text{ mA h g}^{-1}$  at  $0.1 \text{ A g}^{-1}$ ) and outstanding cycling performance (86.6% capacity retention after 2000 cycles at  $1.0 \text{ A g}^{-1}$ ) in AZIBs. It endowed high mass loading, with a high areal capacity ( $0.64 \text{ mA h cm}^{-2}$  at  $0.1 \text{ A g}^{-1}$ ,  $6.0 \text{ mg cm}^{-2}$ ) and a long operational life (1300 cycles with 81.8% capacity retention). Zinc-ion batteries with the MNSMO@CC cathode and Zn@CC anode exhibited good electrochemical performance and flexibility. Notably, synchrotron radiation techniques, molecular dynamics (MD) simulation, and COMSOL Multiphysics simulation were performed for the in-depth analysis of the reaction

kinetics of the MNSMO@CC electrode at the atomic scale. Additionally, the  $\text{Zn}^{2+}$  storage mechanism involving highly reversible intercalation/deintercalation in the  $\delta\text{-MnO}_2$  layer during the charging/discharging process was also thoroughly investigated.

## 2 Results and discussion

### 2.1 Construction of a hierarchical structure and structural characterization

The synthesis mechanism of the composites is shown in Fig. 1a(i). In brief, using CTAB-dissociated  $\text{CTA}^+$  as an intermediate bridge, a 2D layered/3D flower hierarchically structured  $\text{MnO}_2$  was *in situ* grown on modified carbon cloth (MNSMO@CC) *via* molecular assembly and hydrothermal reduction. The function of CTAB is displayed in Fig. 1a(ii). CTAB molecules first dissociate into  $\text{CTA}^+$  and  $\text{Br}^-$  in the solution, with  $\text{CTA}^+$  having a hydrophilic quaternary ammonium head group (electrically positive) and a hydrophobic tail chain.<sup>19,20</sup> At the same time, ionised  $\text{KMnO}_4$  ( $\text{MnO}_4^-$ ) and the modified CC surface with  $-\text{OH}$  and  $-\text{COOH}$  groups are negatively charged.<sup>21</sup> Then, part of the positive hydrophilic group of  $\text{CTA}^+$  shows an affinity for  $\text{MnO}_4^-$ , whereas the excess  $\text{CTA}^+$  adsorbs on the negatively charged CC surface *via* electrostatic interactions. Subsequently, the free  $\text{CTA}^+\text{-MnO}_4^-$  monomers formed nanomicelles *via* a self-assembly strategy, and the tightly packed bilayer anchored on the CC surface *via* hydrophobic interaction of the hydrophobic chain.<sup>22–25</sup> CTAB was thus used as a reducing agent, structure-inducing agent, and growth-inducing agent herein. As CTAB has directional induction properties,  $\text{MnO}_2$  can attach to the CC substrate for the continuous growth, enabling high mass loading on the self-supporting CC electrode. Moreover, different action modes of  $\text{CTA}^+$  at the interface and in solution facilitate the formation of hybrid 2D/3D hierarchically structured  $\text{MnO}_2$ , creating a porous structure for fast ion transport and stable energy storage. To further understand the trapping ability of  $\text{CTA}^+$ , theoretical calculation was performed. Computational results show that the adsorption energy between  $\text{MnO}_4^-$  and  $\text{CTA}^+$  is  $-5.43 \text{ eV}$ , demonstrating a strong interaction that easily captures the  $\text{MnO}_4^-$  to form the molecular complex (Fig. 1a(iii)).<sup>26</sup> In conclusion, CTAB interacts with  $\text{MnO}_4^-$  *via* electrostatic attraction and effectively prevents a strong redox reaction between  $\text{MnO}_4^-$  and CC, avoiding the formation of  $\text{MnO}_2$  composites with a loose structure.

The morphology and structure of the composites were observed by scanning electron microscopy (SEM) and transmission electron microscopy (TEM). The SEM image of the modified CC is shown in Fig. S1.† The SEM images of MNSMO@CC and  $\text{MnO}_2$  combined with CC without adding CTAB (denoted as MO@CC) showed that the  $\text{MnO}_2$  successfully attached to the modified CC (Fig. 1b and S2a†). MO@CC comprises solid particle blocks, whereas MNSMO@CC consists of uniformly grown 3D nanoflower-like spherical particles (Fig. S2b–d†). Note that between the  $\text{MnO}_2$  nanoflower and CC, a 2D carpet-like  $\text{MnO}_2$  layer adheres to the CC surface. This indicates that the  $\text{CTA}^+\text{-MnO}_4^-$  bilayer has successfully changed to carpet-like  $\text{MnO}_2$  in the MNSMO@CC sample (Fig. S3a†). CTAB

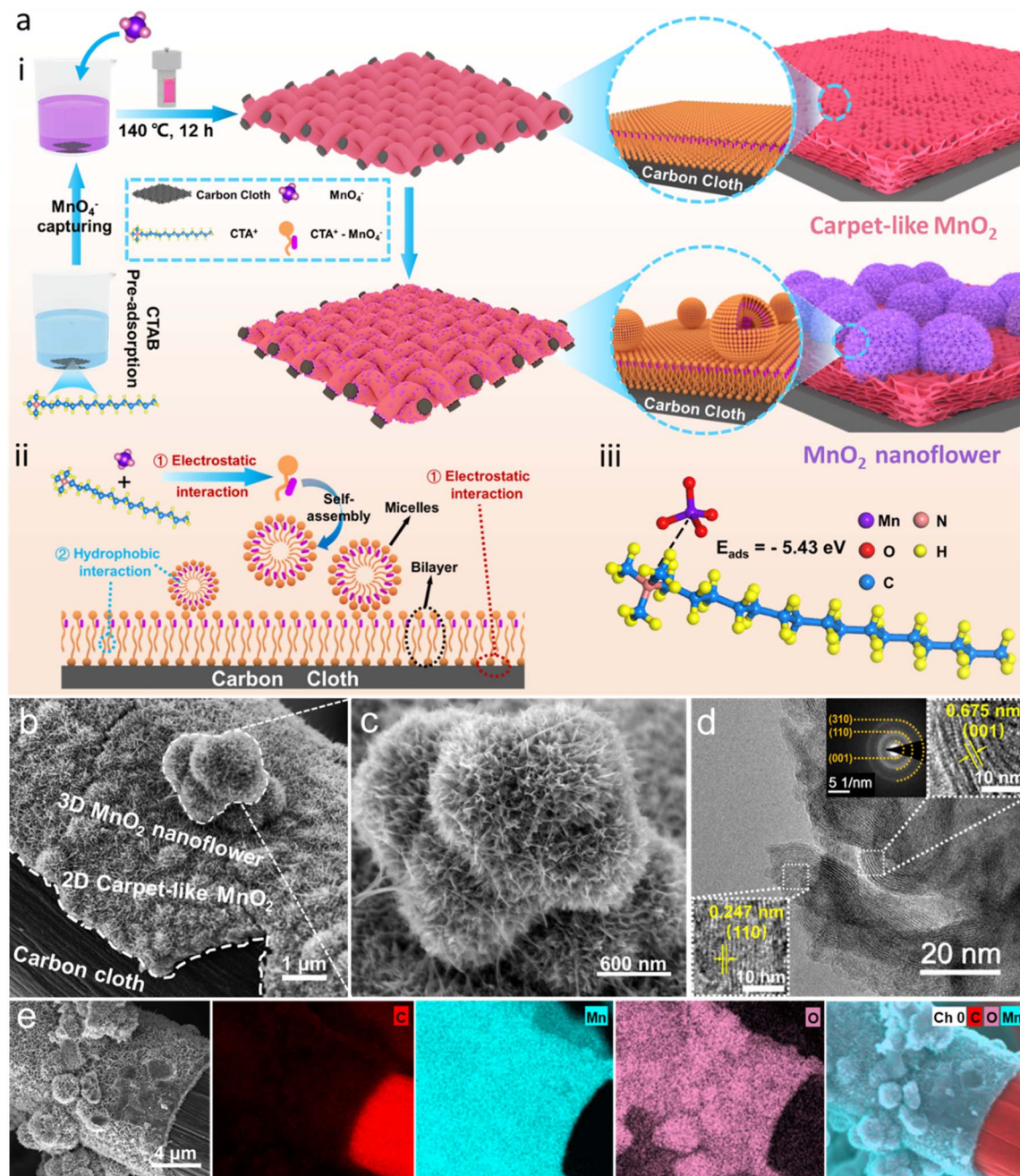


Fig. 1 (a) (i) The synthesis of MNSMO@CC, (ii) the molecular mechanism during the reaction, (iii) the adsorption energy of the  $\text{CTA}^+-\text{MnO}_4^-$  molecule. (b and c) SEM images of MNSMO@CC. (d) TEM image and SAED pattern of MNSMO@CC. (e) EDS mapping images of MNSMO@CC.

functions as a guiding agent, firmly capturing  $\text{MnO}_2$  in the CC fibres and increasing the mass loading of active  $\text{MnO}_2$ . Besides, the higher magnification clearly shows that the hierarchical structure consists of 3D-nanoflower spheres ( $\sim 800 \text{ nm}$ ) and a 2D-carpet-like structure ( $\sim 400 \text{ nm}$ ) in the MNSMO composite, both composed of nanosheets (Fig. 1c and S3b<sup>†</sup>). The  $\text{MnO}_2$  nanosheet in contact with CC effectively increases the number of electron conduction sites and enhances the interface interaction. The thin 2D carpet-like layer provides a short-range electron transmission tunnel, allowing fast electron transfer from the CC to  $\text{MnO}_2$  nanoflower. As a result, the 2D carpet-

like  $\text{MnO}_2$  layer covering the CC surface strengthens the connection of the active material with the CC collector and serves as a conductive medium between the CC skeleton and 3D  $\text{MnO}_2$  nanoflower. In contrast, the  $\text{MO@CC}$  sample without the structure-inducing effect of CTAB shows loose interface contact and a tendency to detach from the CC fibre. A considerably thick  $\text{MnO}_2$  block ( $\sim 1.6 \mu\text{m}$ ) was obtained (Fig. S3c<sup>†</sup>), which increased the electron migration distance and reduced the electrolyte wettability.

A high-resolution TEM image of the MNSMO@CC composite revealed the lattice spacings of 6.75 and 2.47 Å, corresponding



to the (001) and (110) crystal planes of  $\delta\text{-MnO}_2$  (JCPDS 80-1098).<sup>27</sup> The selected area electron diffraction (SAED) pattern of MNSMO@CC shows diffraction rings that match well with the (001), (110) and (310) planes of  $\delta\text{-MnO}_2$  (Fig. 1d).<sup>28,29</sup> The TEM images of  $\text{MnO}_2$  nanoflowers show a visibly 2D nanosheet structure ( $\sim 10$  nm), which concentrates the pore size in the material as the nanosheets grow into a high-dimensional structure (Fig. S4a–c†). This unique pore structure created numerous pathways for  $\text{Zn}^{2+}/\text{H}^+$  ion transfer, enabling high-speed electrode reactions. In contrast, the MO@CC composite exhibits massive stacking and displays the (001) crystal planes of  $\delta\text{-MnO}_2$  (Fig. S4d and e†). However, the sheets are tightly packed together, thereby limiting ion reactions on the  $\text{MnO}_2$  surface and hindering ion diffusion to inner layers. The inverse fast Fourier transform patterns of the white-rectangular area in Fig. 1d and S4e† present the lattice fringes of different crystal planes (Fig. S4f†). The energy dispersive spectroscopy (EDS) mapping of the MNSMO@CC composite shows that Mn and O elements are evenly distributed on the CC fibre, with a clear demarcation from C element (Fig. 1e). This further indicates that the 2D/3D hierarchically structured  $\text{MnO}_2$  was successfully grown on CC, forming a stable self-supporting electrode for high-performance  $\text{Zn}^{2+}$  storage.

The crystal structures of MNSMO@CC and MO@CC were analysed *via* X-ray diffraction (XRD). In Fig. 2a, the diffraction peaks at  $12.5^\circ$ ,  $25.2^\circ$ , and  $37.3^\circ$  are indexed to the (001), (002), and (111) planes of the  $\delta\text{-MnO}_2$  phase (JCPDS 80-1098).<sup>30,31</sup> Compared with those of the standard  $\delta\text{-MnO}_2$  crystal, the diffraction peaks of MNSMO@CC and MO@CC are left shifted, which can be attributed to the layer intercalation of  $\text{K}^+$ .<sup>32</sup> The weak diffraction peaks of  $\text{MnO}_2$  indicate its low crystallinity, possibly caused by the intercalation of  $\text{K}^+$  that created more defects and enlarged the  $\text{MnO}_2$  layer spacing.<sup>30</sup> The larger radius of  $\text{K}^+$  compared with  $\text{Zn}^{2+}$  expands the layer spacing of  $[\text{MnO}_6]$ , providing sufficient space for  $\text{Zn}^{2+}/\text{H}^+$  diffusion in the  $\delta\text{-MnO}_2$  crystal. The Raman spectra reveal  $\nu_1$  and  $\nu_2$  characteristic peaks at  $572$  and  $628\text{ cm}^{-1}$ , respectively, corresponding to the  $d_{x^2-y^2}$  and the  $d_{x^2-y^2}$  orbitals of the Mn–O band in  $[\text{MnO}_6]$  basal octahedra (Fig. S5†).<sup>33</sup> Compared with the MO@CC sample, the decreased intensity of these peaks in MNSMO@CC is closely related to the effective changes in the covalent interaction between Mn–O layers following the creation of various oxygen vacancies.<sup>34,35</sup>

The  $\text{N}_2$  adsorption–desorption isotherms of MNSMO@CC and MO@CC show the characteristic of mesoporous materials with the type-IV adsorption isotherm, including an obvious H3-type hysteresis loop (Fig. S6a and b†).<sup>36,37</sup> However, the type-I adsorption isotherm was attained in the MNSMO@CC sample at a low-pressure range ( $P/P_0 = 0.005\text{--}0.01$ ), attributed to the filling of micropores. The pore size distribution of MNSMO@CC displays micropores and mesopores, demonstrating a hierarchical porous structure, while MO@CC exhibits a single mesoporous structure (Fig. 2b).<sup>38</sup> The unique porous structure of MNSMO@CC ensured rapid electrolyte permeation and accelerated the electrochemical reaction. Different pore structures effectively promoted the  $\text{Zn}^{2+}/\text{H}^+$  transport, thereby the mass transfer rate was successfully improved.

The X-ray photoelectron spectroscopy (XPS) spectra in Fig. S7a† show the signal peaks of C, Mn, O and K. The Mn 3s peak distance was used to calculate the average oxidation state (AOS) for gaining the chemical valence of  $\delta\text{-MnO}_2$  (Fig. S7b†). Thence, the AOS of Mn in MNSMO@CC is 3.30, which is lower than that in MO@CC (3.55). This decrease was ascribed to the charge compensation from oxygen defects, confirming the modification of the nanomicelle-induced material. The doublet in K 2p spectra evidences the intercalated  $\text{K}^+$  in  $\delta\text{-MnO}_2$  (Fig. S7c†).<sup>39</sup> The XPS spectrum of Mn 2p presents a pair of peaks, including those of Mn  $2p_{3/2}$  ( $642.48\text{ eV}$ ) and Mn  $2p_{1/2}$  ( $654.18\text{ eV}$ ), which was confirmed to be the characteristics of the  $\text{MnO}_2$  phase (Fig. 2c).<sup>15</sup> These peaks in MNSMO@CC slightly shifted to a lower position compared with MO@CC, possibly due to the generation of oxygen vacancies and charge interaction between  $\delta\text{-MnO}_2$  and CC. In the O 1s XPS spectra, the defective oxygen peak intensity of MNSMO@CC was higher than that of MO@CC, reflecting a higher concentration of oxygen vacancies. Furthermore, the Mn–O–Mn bonding in MNSMO@CC showed lower intensity, originating from the Mn–O lattice distortion induced by the loss of lattice oxygen (Fig. S7d†).<sup>40</sup>

X-ray absorption near edge structure (XANES) spectra of the normalised Mn K-edge were analysed to delve deeper into the local atomic structure of the Mn atom (Fig. 2d). The main absorption edge of MNSMO@CC was compared with those of three standard manganese oxides with different chemical states (Mn(II), Mn(III), and Mn(IV)). The K-edge of MNSMO@CC was located between those of standard  $\text{Mn}_2\text{O}_3$  and  $\text{MnO}_2$ , indicating an oxidation state between Mn(III) and Mn(IV); these observations were consistent with the XPS results.<sup>41,42</sup> Moreover, the R-space spectra of MNSMO@CC exhibit prominent peaks at  $1.4$  and  $2.4\text{ \AA}$ , corresponding to the Mn–O bond and the Mn–Mn coordination shell (Fig. S8†).<sup>43</sup> Compared with the standard  $\text{MnO}_2$ , the Mn–Mn peak intensity considerably increased in MNSMO@CC, which indicated an improved Mn coordination environment. This improvement enhanced the degree of orbital hybridization and the electrical conductivity of the MNSMO@CC composite. To more clearly illustrate the local coordination environment of Mn, the contour plots of MNSMO@CC were visualised by using wavelet transform (WT) (Fig. 2e and f). The WT contour plots of MNSMO@CC show characteristics resembling those of the standard  $\text{MnO}_2$  structure, particularly the two WT maxima, suggesting an analogous local structure in both the samples. However, MNSMO@CC shows higher intensity at larger  $k$ -space, indicating more corner-sharing Mn–Mn in MNSMO@CC, consistent with the previous results. The molecular manipulation effectively builds the  $\text{MnO}_2$ –CC interface connection, alleviating electrostatic interactions to accelerate ionic transport dynamics and maintain structural stability during the electrochemical process. Consequently, more active sites were exposed, which increased the durable capacity of AZIBs. To further elucidate the effect of adding CTAB to the material, Kelvin probe force microscopy (KPFM) was employed for measuring the surface potential. The contact potential difference (CPD) of the two samples is shown in Fig. 2g. MNSMO@CC exhibited a CPD of  $64.7\text{ mV}$ , exceeding that of MO@CC ( $56.4\text{ mV}$ ). This indicates a stronger built-in

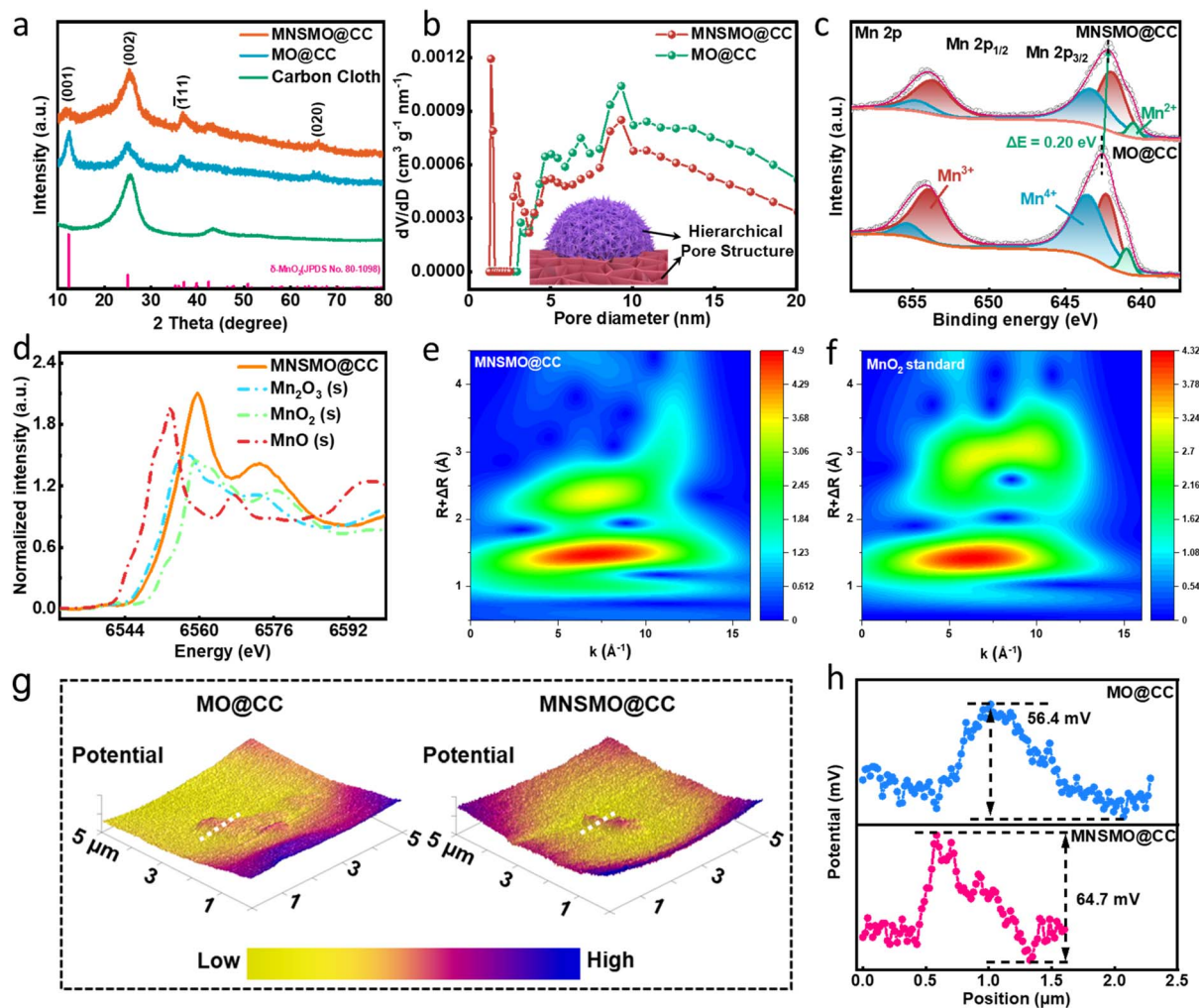


Fig. 2 (a) XRD pattern, (b) corresponding pore size distribution, and (c) high-resolution XPS spectra of Mn 2p of MNSMO@CC and MO@CC. (d) XANES spectra of MNSMO@CC and three standard oxides ( $\text{MnO}$ ,  $\text{Mn}_2\text{O}_3$ , and  $\text{MnO}_2$ ). (e and f) EXAFS wavelet transformation contour plots of MNSMO@CC and standard  $\text{MnO}_2$ . (g) 3D CPD contour projects and (h) the corresponding line-scan CPD distribution curves of MNSMO@CC and MO@CC.

electric field within MNSOM@CC, promoting the transport of electrolyte ions (Fig. 2h).<sup>44</sup>

## 2.2 Battery electrochemical performance

AZIBs were assembled to investigate the electrochemical properties of MNSMO@CC and MO@CC samples. Cyclic voltammograms of MNSMO@CC show two couples of redox peaks at 1.60/1.56 V and 1.39/1.27 V, respectively (Fig. 3a). The MNSMO@CC electrode had a higher current response and a wider voltammogram area compared with the MO@CC electrode, and the MNSMO@CC electrode displays smaller voltage polarization than that of the MO@CC electrode, demonstrating a high reversibility (Fig. 3b).<sup>45</sup> The galvanostatic charge-discharge (GCD) profiles in Fig. 3c reveal that MNSMO@CC shows a more stable and extended discharge plateau to achieve a higher specific capacity. Meanwhile, a discharge/charge plateau at  $\approx 1.40/1.60$  V (vs.  $\text{Zn}^{2+}/\text{Zn}$ ) is detected, consistent with the cyclic voltammetry (CV) profiles. The discharge

plateaus corresponding to different material reactions are shown in Fig. S9.† With increased scan rate, the CV curves of the MNSMO@CC electrode exhibit a slight peak shift, mainly attributed to polarization during  $\text{Zn}^{2+}$  intercalation/deintercalation (Fig. S10a†).<sup>29</sup> Furthermore, the relationship between scan rate ( $\nu$ ) and peak current ( $i$ ) was analysed to describe the kinetically controlled electrode reaction process. As shown in Fig. S10b,† the fitting curves show a good linear relationship. The  $b$  values of MNSMO@CC are 0.653, 0.541, 0.734 and 0.683, demonstrating that the charge storage process is governed by diffusion and capacitive behaviour. To further explore diffusion-controlled and capacitive reactions, the pseudo-capacitance contribution was calculated.<sup>15</sup> Fig. 3d shows the capacitance contribution rate of MNSMO@CC increases from 23.9% to 56.0% with increasing scan rate, illustrating that the charge storage process is primarily diffusion-controlled.<sup>46</sup> The diffusion contribution of MO@CC is considerably lower than that of MNSMO@CC, indicating that

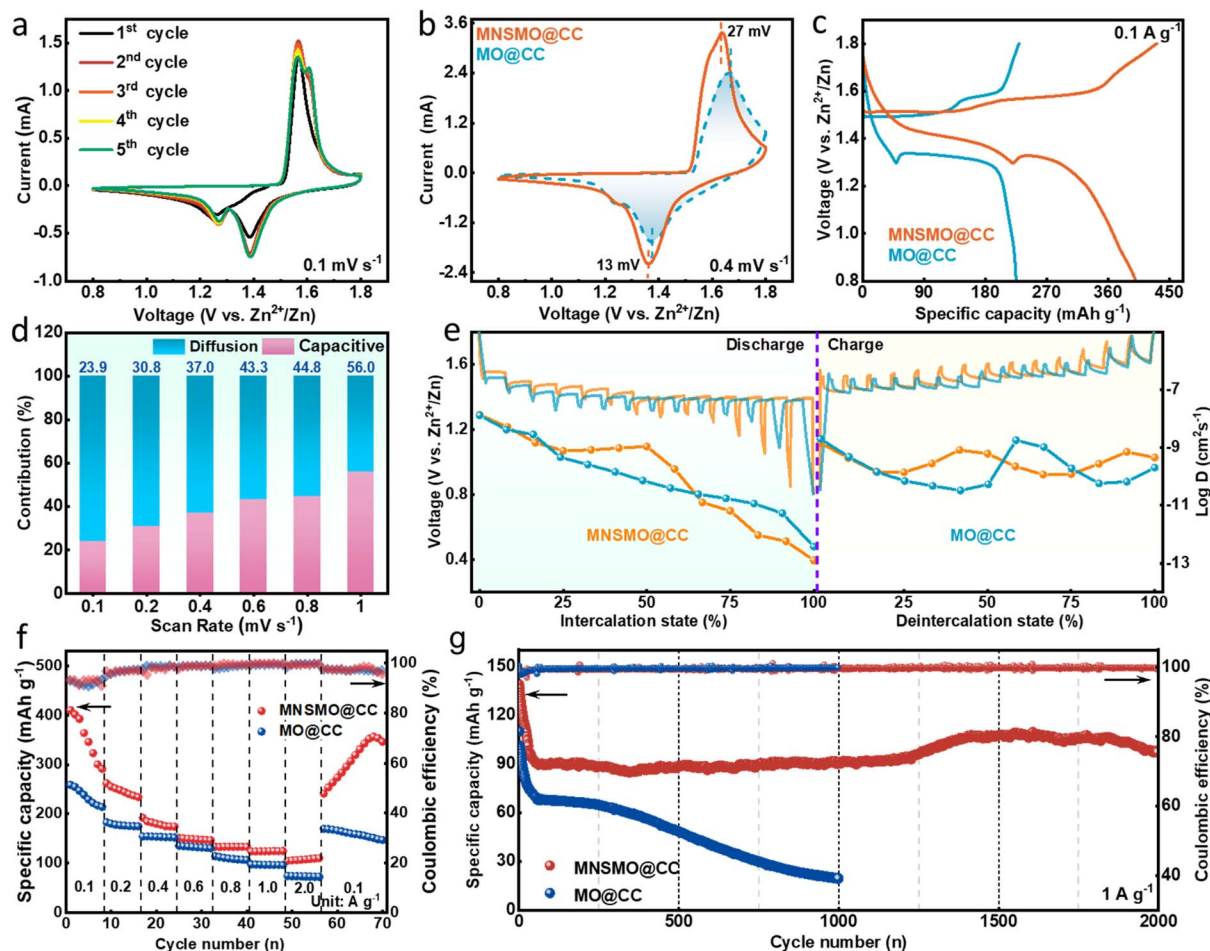


Fig. 3 (a) The MNSMO@CC electrode's first five CV curves at 0.1 mV s<sup>-1</sup>. (b) CV curves and (c) GCD curves of the MNSMO@CC and MO@CC electrodes. (d) Diffusion coefficient values calculated for MNSMO@CC. (e) GITT curves and the corresponding diffusion coefficients at the discharge/charge states of the MNSMO@CC and MO@CC electrodes. Comparison plot of the electrochemical performance of MNSMO@CC and MO@CC. (f) Rate performance at the current densities ranging from 0.1 to 2 A g<sup>-1</sup>, (g) the long-term cycling performance at 1 A g<sup>-1</sup>.

the hierarchical structure integrated with the 2D nanosheet has generated abundant channels for ion transfer to facilitate electrode reaction (Fig. S11†).

The galvanostatic intermittent titration technique (GITT) was performed to evaluate the cation-diffusion coefficient ( $D$ ) (Fig. 3e). The  $D$  in the MNSMO@CC electrode was  $10^{-8}$ – $10^{-13}$  cm<sup>2</sup> s<sup>-1</sup>, which was higher than that of the MO@CC electrode.<sup>47</sup> Electrochemical impedance spectroscopy (EIS) revealed that the charge transfer resistance ( $R_{ct}$ ) of MNSMO@CC was significantly lower than that of MO@CC (Fig. S12†). The 2D carpet-like MnO<sub>2</sub> facilitated an outstanding electrical conductivity between MnO<sub>2</sub> 3D nanoflowers and CC, and K<sup>+</sup> insertion enlarged the layer space of  $\delta$ -MnO<sub>2</sub>, resulting in high-speed Zn<sup>2+</sup>/H<sup>+</sup> ion transport. The MNSMO@CC electrode showed high specific capacities of 409.6, 262.1, 192.0, 151.2, 133.5, 123.8 and 104.9 mA h g<sup>-1</sup> at current densities of 0.1, 0.2, 0.4, 0.6, 0.8, 1.0, and 2.0 A g<sup>-1</sup>, respectively (Fig. 3f). In particular, the MNSMO@CC electrode regained its capacity when the current density returned to 1.0 A g<sup>-1</sup>, indicating its excellent rate performance as well as high reversibility. In contrast, the MO@CC electrode showed lower specific capacities of 254.6 mA h g<sup>-1</sup> at 0.1 A g<sup>-1</sup>

and 99.1 mA h g<sup>-1</sup> at 2.0 A g<sup>-1</sup>. The high specific capacity of MNSMO@CC could be attributed to the distinct electron shuttle structure formed by the 2D/3D structural materials on the CC fibres. The 2D carpet-like surface resolutely anchored on the fibre and its upper surface, unified by a nanosheet, generates numerous active sites with 3D  $\delta$ -MnO<sub>2</sub> nanoflowers. This configuration enabled rapid electron transfer and high-rate ion storage.

To reveal the application potential of the AZIBs, long-term cycling performance was measured (Fig. 3g). After 10 cycles of activation, the MNSMO@CC electrode showed a specific capacity of 121.2 mA h g<sup>-1</sup> at 1 A g<sup>-1</sup>. In the subsequent process, the MNSMO@CC electrode exhibited a high capacity retention of 86.6% after 2000 cycles, which is superior to that of the MO@CC electrode. This result demonstrates the key role of CTAB in establishing a strong connection between MNSMO and the CC collector. This robust interface effectively anchors  $\delta$ -MnO<sub>2</sub> nanoparticles, preventing the detachment of high-loading active  $\delta$ -MnO<sub>2</sub> during electrochemical reactions. The cooperative effect of nanosheet morphology and hierarchical structure yielded the MNSMO@CC electrode with a porous



structure for achieving reversible insertion and extraction. The electrolyte soaking experiment of the two electrodes was performed as shown in Fig. S13.† After 30 days of soaking, the solution remained clear in the MNSMO@CC sample, indicating the effective suppression of the Jahn–Teller effect. This suppression was caused by the inherent flexibility of the CC substrate, which alleviated morphological and structural strain on MNSMO during the charge and discharge processes. Conversely, the electrolyte in which MO@CC was soaked changed to brown, indicating that  $\text{MnO}_2$  had dissolved. In conclusion, the micro/mesoporous structure provided abundant pathways for the efficient diffusion of  $\text{Zn}^{2+}/\text{H}^+$  ions. As a result, the hierarchical  $\delta\text{-MnO}_2$  structure could fully contact the electrolyte, exhibiting excellent specific capacity. Furthermore, the modified CC provided a flexible substrate to mitigate the mechanical strain of  $\delta\text{-MnO}_2$  during electrochemical reactions. This synergy enabled the electrode to maintain stable cycling performance over time.

The active mass loading of the electrode has a great effect on the areal capacity.<sup>48</sup> Attaining a high-mass-loading electrode by customizing  $\delta\text{-MnO}_2$  on a self-supporting current collector has been proven to be readily achievable. Therefore, high  $\text{MnO}_2$  loading MNSMO@CC was fabricated. As shown in Fig. 4a, when the mass loading increases to  $6.1 \text{ mg cm}^{-2}$ , the areal capacity of the MNSMO@CC electrode reaches  $0.64 \text{ mA h cm}^{-2}$  at  $0.1 \text{ A g}^{-1}$ . The electrode was tested at different current densities and ultimately at  $0.1 \text{ A g}^{-1}$ , during which it exhibited good reversibility. Moreover, when the mass loading is about  $6.0 \text{ mg cm}^{-2}$ , an 81.8% capacity retention was achieved after 1300 cycles at  $0.8 \text{ A g}^{-1}$ . Owing to the effect of the flexible CC substrate,  $\text{MnO}_2$

lattice strain during ion intercalation was relaxed. This further demonstrated that the self-supporting MNSMO@CC electrode with a 2D/3D hierarchical structure has the advantage of high electrochemical stability (Fig. 4b). Different materials used in AZIBs were compared, which showed that the MNSMO@CC electrode exhibited higher areal capacity at different current densities. This confirmed its superior performance under high-mass-loading conditions (Fig. 4c and Table S1†).

To assess the feasibility of practical application of the electrode, a flexible AZIB pouch cell was assembled (Fig. 4d(i)). The positive electrode was fabricated using MNSMO@CC with a mass loading of  $7.4 \text{ mg cm}^{-2}$  (Fig. S14a†), and the negative electrode was prepared by electroplating Zn onto the CC (Fig. S14b†) using a glass fibre (GF) separator (Fig. S14c†). The resulting  $\text{Zn@CC}||\text{MNSMO@CC}$  pouch cell (Fig. S14d†) exhibited excellent continuous power supply capabilities, and powered a digital clock easily and continuously for 12 h (Fig. 4d(ii)). Also, the pouch cell can light up the digital clock under the bending states of  $45^\circ$  and  $135^\circ$ , revealing its foldability (Fig. 4d(iii)). These successful experimental results underscore the potential of MNSMO@CC for applications in flexible and wearable electronics.

### 2.3 Electrode reaction mechanism

To investigate the structural evolution of the MNSMO@CC electrode during the charge and discharge processes, *ex situ* characterisation was performed. Fig. S15a† displays the GCD profile for the nine states of  $\text{Zn/MNSMO@CC}$  batteries at  $0.1 \text{ A g}^{-1}$ . The *ex situ* XRD patterns at different voltage states

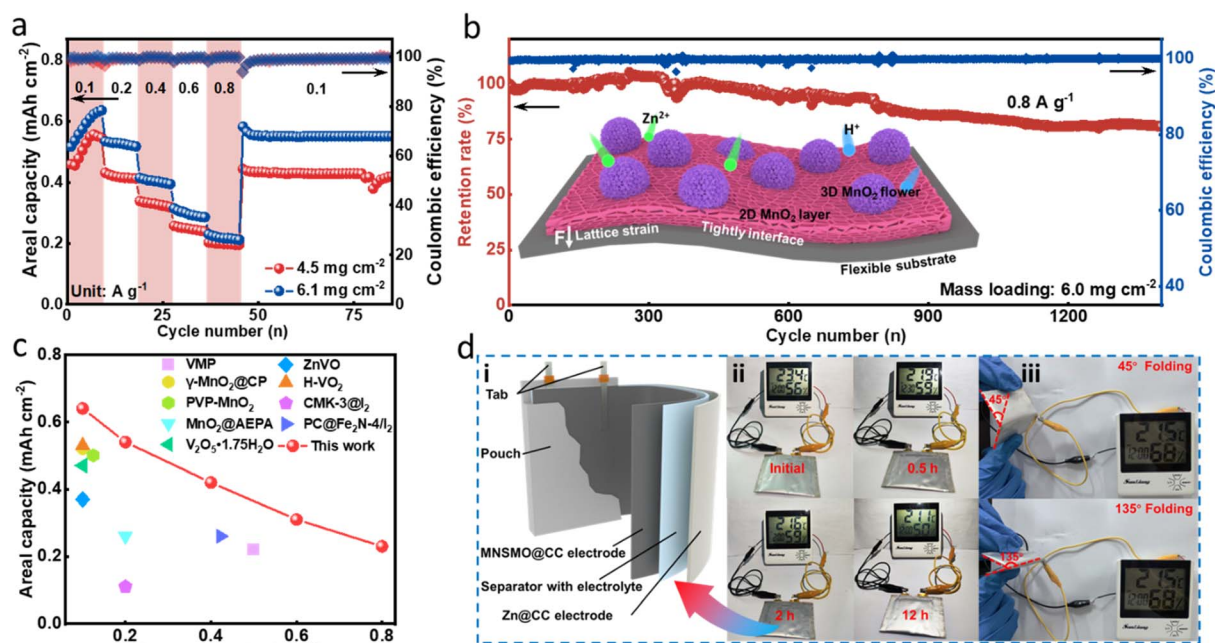


Fig. 4 Electrochemical evaluation of the  $\text{Zn/MNSMO@CC}$  batteries at high active mass loadings. (a) Rate performance. (b) Long-term cyclabilities of the  $\text{Zn/MNSMO@CC}$  batteries at  $0.8 \text{ A g}^{-1}$ . (c) Comparison of the areal capacity of the high-mass-loading MNSMO@CC electrode with that of previously reported electrodes. (d) Application of the pouch cell. (i) Schematic illustration of a  $\text{Zn@CC}||\text{MNSMO@CC}$  pouch cell. (ii) Photos of a pouch cell device powering a digital clock. (iii) Flexibility tests of the pouch cell under different bending conditions.

during the initial cycles are presented in Fig. 5a and S15b.† Upon cycling, new diffraction peaks emerge at  $12.3^\circ$ ,  $32.7^\circ$ ,  $35.1^\circ$  and  $59.9^\circ$ , which can be attributed to the characteristic peaks of  $\text{Zn}_4\text{SO}_4(\text{OH})_6 \cdot 0.5\text{H}_2\text{O}$  (ZHS; JCPDS 44-0674).<sup>7</sup> This result indicates that the ZHS deposits/dissolves on the electrode during the discharge/charge process. The  $\text{H}^+$  intercalation in the cathode changes the local pH on the electrode surface during electrode reaction, causing the reversible formation and disappearance of ZHS. Throughout the charge/discharge cycle, the crystal structure of MNSMO@CC undergoes minimal changes compared with that of its pristine state. This indicates that the  $\text{K}^+$  intercalated  $\delta\text{-MnO}_2$  offers a large ion transfer pathway for fast cation transport.<sup>46</sup>

*Ex situ* XPS analysis was conducted to verify the changes in element valence of MNSMO@CC during ion intercalation and extraction. When the voltage was increased to 1.8 V and decreased to 0.8 V, the peaks of Zn 2p split into Zn  $2p_{1/2}$  and Zn  $2p_{3/2}$  and their intensity gradually decreased. It then returned to a higher peak response, corresponding to  $\text{Zn}^{2+}$  intercalation into the  $\delta\text{-MnO}_2$  layer in the MNSMO@CC electrode (Fig. S16†). Meanwhile, the high-resolution Mn 2p spectra at different voltage states are shown in Fig. 5b. At the 1st discharge state of

0.8 V, a new peak of  $\text{Mn}^{2+}$  appears at 640.9 eV, indicating that a small amount of  $\text{Mn}^{3+}$  and  $\text{Mn}^{4+}$  reduced to a lower valence. When fully charged to 1.8 V, the extraction of  $\text{Zn}^{2+}$  from the layered structure significantly augmented the peak integral areas of  $\text{Mn}^{3+}$  and  $\text{Mn}^{4+}$ . During the 2nd cycle, when the electrode was fully discharged to 0.8 V, the peak intensities of  $\text{Mn}^{3+}$  and  $\text{Mn}^{4+}$  obviously diminished, which further substantiated the reaction of  $\text{Mn}^{3+}$  and  $\text{Mn}^{4+}$  caused by  $\text{Zn}^{2+}$  insertion.<sup>49</sup> The O 1s spectrum shows the maximum fitting peaks of ZHS at 532.9 eV, which indicates the reversible deposition/dissolution of ZHS during the electrochemical process (Fig. 5c).<sup>50</sup> Moreover, the characteristic bands of the Mn–OH bond corresponded to the peak observed at 531.5 eV. And the peaks at 529.9 eV were fitted to the Mn–O–Mn bond in  $\delta\text{-MnO}_2$ . During electrochemical cycling, the insertion of  $\text{Zn}^{2+}/\text{H}^+$  maximised the ZHS and Mn–OH fitting peaks. When the battery voltage reached 1.8 V, the peak intensity of the Mn–O–Mn bond was strengthened due to the extraction of electrolyte ions.<sup>51</sup> This absorption/desorption mechanism of  $\text{Zn}^{2+}/\text{H}^+$  corroborated with the XRD analysis results.

The reversible formation of ZHS at different voltages was further verified by *ex situ* SEM (Fig. 5d). In the pristine state

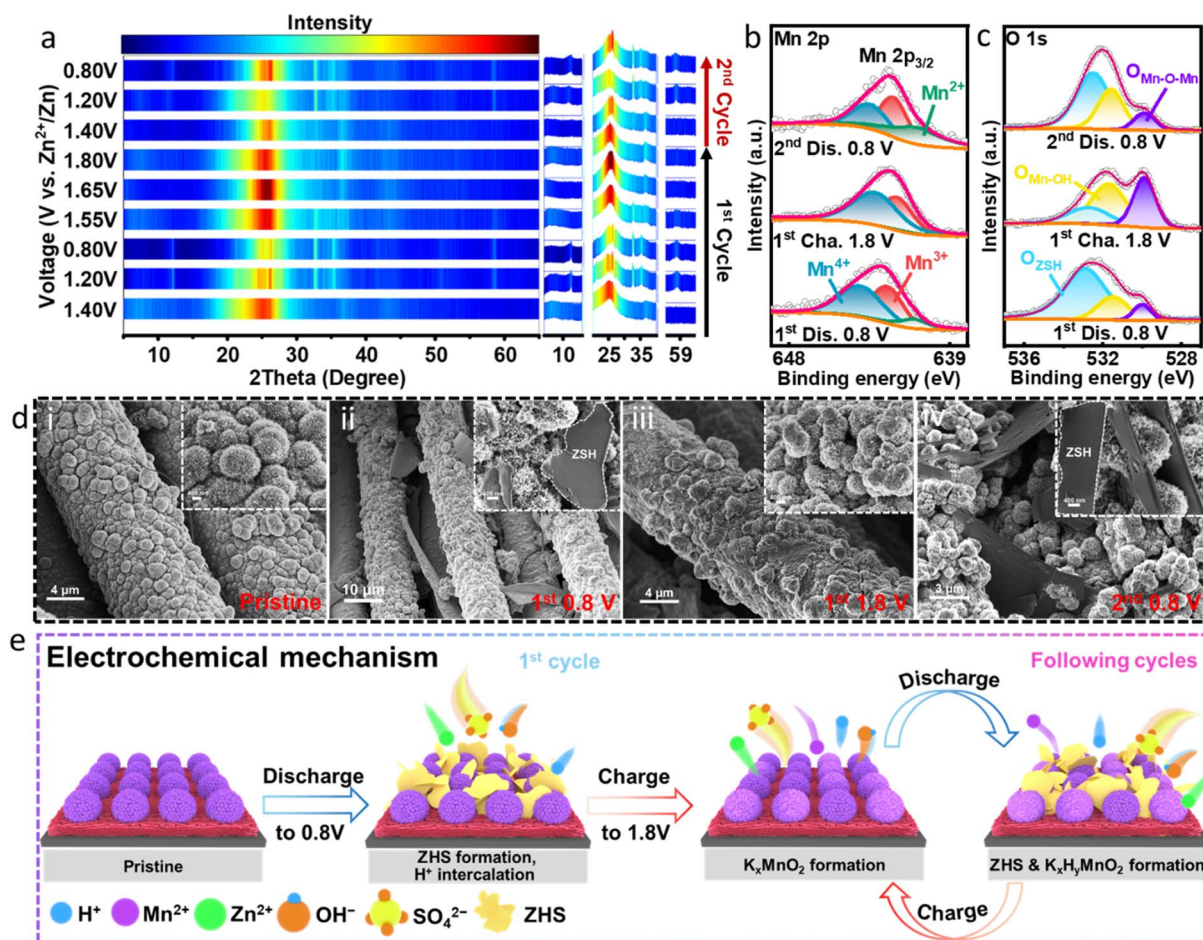
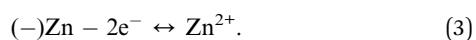
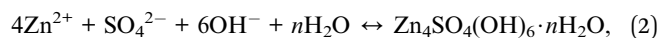
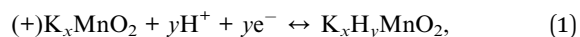


Fig. 5 (a) *Ex situ* XRD patterns of the MNSMO@CC electrode collected at specific voltage states. *Ex situ* XPS of (b) Mn 2p and (c) O 1s, and (d) *ex situ* SEM of the MNSMO@CC electrode in different voltage states. (e) Schematic diagram of the aqueous Zn/MNSMO@CC battery storage mechanism.



(Fig. 5d(i)), the SEM images show the hierarchical structure of MNSMO@CC. However, after discharging to 0.8 V (Fig. 5d(ii)), some flakes were formed on the surface of the MNSMO@CC electrode, which corresponded to the ZHS phase. Subsequently, the ZHS phase continuously disappeared and appeared during the subsequent charge/discharge cycles (Fig. 5d(iii) and (iv)). This phenomenon corresponded to the changes in the *ex situ* XRD characteristic peaks at different voltages. Noteworthily, the nanosheet morphology of MNSMO@CC remained stable during the initial electrochemical cycling. This phenomenon highlighted that the combination of CC and  $\delta$ -MnO<sub>2</sub> effectively improved the electrode reaction kinetics and mitigated the interface stress caused by the structural evolution of MnO<sub>2</sub>. As a result, the electrode maintained a good structural morphology and provided a solid foundation for subsequent long cycling.

Fig. 5e shows the Zn<sup>2+</sup> storage mechanism of the MNSMO@CC electrode in the battery. During the discharge, H<sup>+</sup> ions diffuse into the hierarchically structured  $\delta$ -MnO<sub>2</sub>, forming abundant OH<sup>-</sup> on the MNSMO@CC cathode surface. Consequently, SO<sub>4</sub><sup>2-</sup> and Zn<sup>2+</sup> in the electrolyte combined with OH<sup>-</sup> and rapidly deposited the ZHS sheets on the MNSMO@CC surface.<sup>52,53</sup> In contrast, when charged to a high potential, H<sup>+</sup> was deintercalated from the hierarchical porous structure, accompanied by the dissolution of ZHS sheets. The high reversibility of ion intercalation and extraction reflected stable electrolyte ion transport in the K<sup>+</sup> pre-intercalation of  $\delta$ -MnO<sub>2</sub>. Although some by-products, such as MnOOH, were deposited/dissolved on the MNSMO@CC cathode surface, the overall structure remained unchanged.<sup>54</sup> These reversible electrochemical processes effectively improved the battery performance. In summary, the reaction of the MNSMO@CC cathode in batteries can be described as follows:<sup>46,54</sup>



Multiphysics simulation is employed to clarify the advantages of the carpet-like MnO<sub>2</sub> structure during electrode reaction. Fig. S17a† shows the simulating electrode model, and Fig. S17b† shows its cross-sectional view. When the electrode was under a current density of 1 mA cm<sup>-1</sup>, the simulation results of the electric field (Fig. 6a(i)) revealed that the highest potential was predominantly distributed at the CC. The electric field direction extended from the CC towards the outer MnO<sub>2</sub> layer. This potential gradient facilitated the directional transfer of electrons from the current collector to the active material. The images of charge distribution (Fig. 6a(ii)) indicate that electric charge was distributed mainly on the cladding MnO<sub>2</sub>. The pronounced electric field attracted Zn<sup>2+</sup> ions directionally to the electrode interface, and the differential electric charge distribution enhanced the conductivity of the high-dimensional structure, boosting the Zn<sup>2+</sup> reaction kinetics on the porous structure.<sup>55,56</sup> The displacement section (Fig. 6a(iii)) indicated that the deformation of MNSMO@CC primarily occurred at the

outer MnO<sub>2</sub> layer, whereas the inner CC skeleton underwent minimal deformation. The temperature distribution in the sectional part (Fig. 6a(iv)) was uniform, which contributed to the thermal stability of the MNSMO@CC electrode during battery operation. These simulations indicated that the flexible CC could act as an elastic base to dissipate stress and provide superior mechanical properties for high-mass-loading active MnO<sub>2</sub> reactions.<sup>57</sup> Consequently, it is anticipated that stress dissipation can effectively inhibit MnO<sub>2</sub> dissolution and decrease the Jahn–Teller distortion, thereby helping the battery to achieve long-term cycling.

Density functional theory (DFT) calculations were employed to elucidate performance variations resulting from intercalated ions and heterogeneous recombination. The optimised models of  $\delta$ -MnO<sub>2</sub>, K<sup>+</sup>-intercalated  $\delta$ -MnO<sub>2</sub> (K-MnO<sub>2</sub>), and K<sup>+</sup>-intercalated  $\delta$ -MnO<sub>2</sub>/CC (K-MnO<sub>2</sub>@CC) are shown in Fig. S18.† Fig. 6b shows the calculated total density of states (DOS) of  $\delta$ -MnO<sub>2</sub>, K-MnO<sub>2</sub>, and K-MnO<sub>2</sub>@CC. Impressively, K-MnO<sub>2</sub> and K-MnO<sub>2</sub>@CC exhibited a continuous and increased DOS near the Fermi level at the dotted line, revealing that the intercalated ions and CC composite decreased the bandgap of materials.<sup>58</sup> Moreover, the analysis of partial density of states (PDOS) in Fig. 6c revealed that the d-band centre of Mn in K-MnO<sub>2</sub>@CC exhibited a noticeable upshift towards the Fermi level compared with that in  $\delta$ -MnO<sub>2</sub>.<sup>59</sup> This observation further confirmed the abundance of active electron states in proximity to the Fermi level, indicating enhanced charge delocalisation. Such conditions are conducive to efficient charge transfer, thereby catalysing electrolysis dynamics.<sup>59,60</sup> Based on the ball and stick model of K-MnO<sub>2</sub>@CC (Fig. 6d), the intercalation of K<sup>+</sup> into  $\delta$ -MnO<sub>2</sub> expanded the interlayer spacing and provided optimal conditions for the rapid diffusion of electrolyte ions. Moreover, the stable two-phase interface formed between  $\delta$ -MnO<sub>2</sub> and CC created an interfacial synergy, thereby forming a fast electron transport channel. This considerably enhanced the electrode conductivity, thereby increasing the efficiency of the electrochemical reaction. Molecular dynamics (MD) simulation was performed to compare the diffusion rate of Zn<sup>2+</sup> in the two electrode systems with different interfacial distances. The simulation boxes comprising the electrolyte and electrode materials at the original state are shown in Fig. 6e and f. As shown in Fig. 6g, the value of  $D_{Zn^{2+}}$  ( $1.803 \times 10^{-3}$  cm<sup>2</sup> s<sup>-1</sup>) in the short-distance model is higher than that of the long-distance model ( $1.580 \times 10^{-3}$  cm<sup>2</sup> s<sup>-1</sup>). This result confirms that the bridging function of CTAB allowed MnO<sub>2</sub> to grow tightly in the CC, thereby decreasing the distance between the two phases and realising strong Zn<sup>2+</sup> diffusion kinetics.<sup>61–63</sup>

The simulation and calculation results collectively highlighted the feasibility of the molecular manipulation strategy for improving the properties of MNSMO@CC composites. The molecular attraction strategy successfully reduced the distance at the CC–MnO<sub>2</sub> heterogeneous interface, whereas K<sup>+</sup> intercalation created ample space for the movement of ions and facilitated high-speed electrolyte transfer. The 2D carpet-like MnO<sub>2</sub> layer, combined with CC fibres, formed a short interface distance, establishing a rapid electron transmission tunnel between the two phases. This not only enhanced the material's

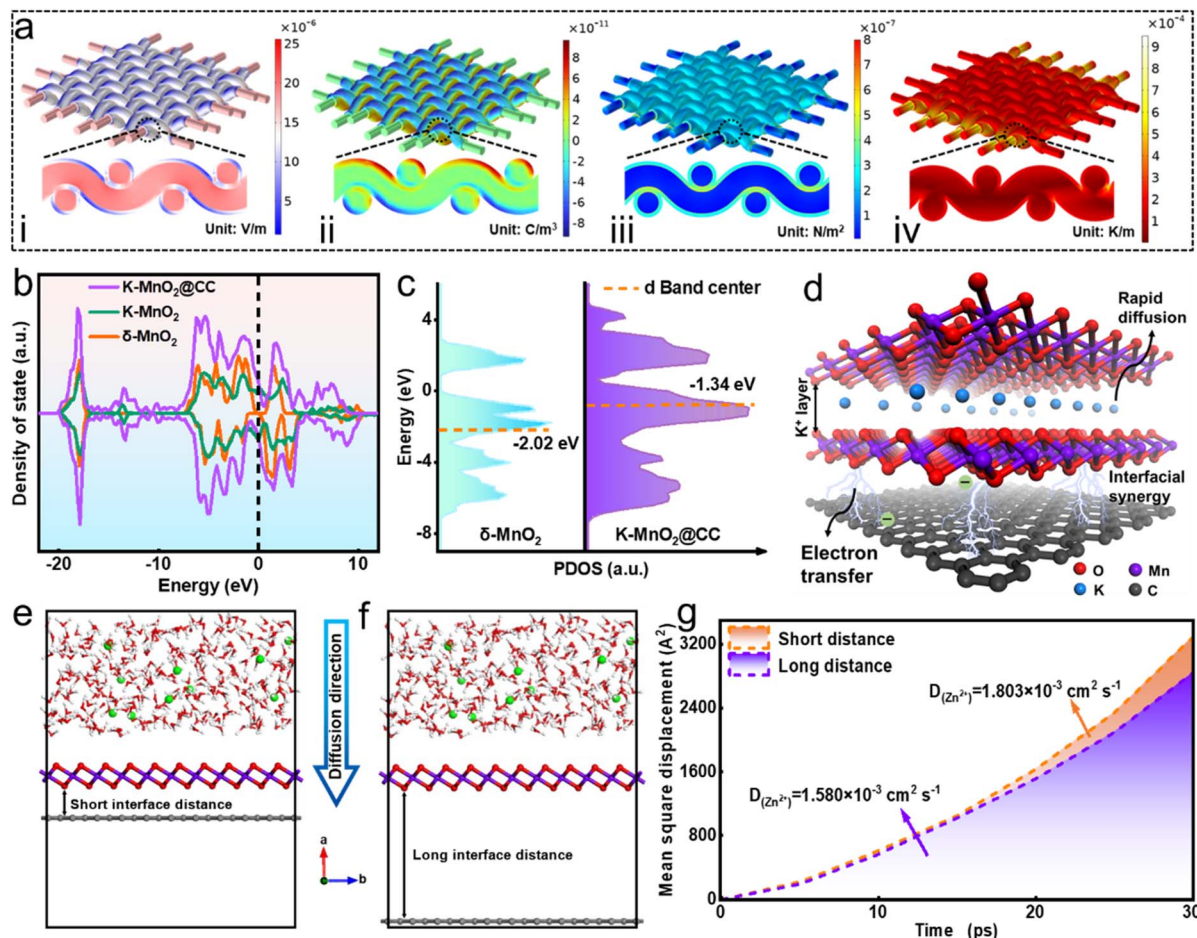


Fig. 6 (a) COMSOL Multiphysics simulation of (i) electric field, (ii) charge density distribution, (iii) structure deformation, and (iv) temperature difference of  $\text{MnO}_2\text{@CC}$ . (b) PDOS and the band center relative to the Fermi level of  $\delta\text{-MnO}_2$  and  $\text{K-MnO}_2\text{@CC}$  samples. (c) D-band center of Mn. (d) Visualization schematic of the ball and stick model of  $\text{K-MnO}_2\text{@CC}$ . (e) and (f) initial MD simulation models for  $\text{Zn}^{2+}$  diffusion in different  $\text{MnO}_2$ -carbon interface distance samples. (g) Overall  $\text{Zn}^{2+}$  diffusion coefficient.

conductivity but also effectively mitigated  $\delta\text{-MnO}_2$  stress during electrochemical reactions. Consequently, the  $\text{MNSMO@CC}$  electrode exhibited outstanding specific capacity and stable cycling performance.

### 3 Conclusions

A reasonable design concept aimed at promoting the integration of two-phase interfaces *via* a nanomicelle-induced strategy was proposed herein. This strategy enabled the electrostatic adsorption and self-assembly of CTAB to anchor the hierarchically structured  $\text{MnO}_2$  on CC for fabricating a self-supporting electrode. This innovative approach highlighted the potential of robust  $\text{MNSMO@CC}$  electrode materials for use in AZIBs, thereby expanding their applicability to  $\text{MnO}_2$  and CC hetero-interfaces. Results revealed the proposed strategy to be a universal methodology. The  $\text{MNSMO@CC}$  electrode displays exceptional capability to store  $\text{Zn}^{2+}$  and achieved a high specific capacity of  $409.6 \text{ mA h g}^{-1}$  at  $0.1 \text{ A g}^{-1}$ . In addition, it exhibits a stable cycling performance, with a retention rate of 86.6% at  $1 \text{ A g}^{-1}$  after 2000 cycles. Furthermore, a high-mass-loading

electrode was tested and integrated into a flexible pouch cell to evaluate its practical applicability. This study combines MD and COMSOL Multiphysics simulations to elucidate the structure-activity mechanism underlying these special results. Also, XANES and *ex situ* characterisation were employed to determine the compositional and structural changes at the interface at multiple scales. This study thus presented a reliable perspective on using molecular modulation to enhance the storage capacity by constructing a hierarchically structured  $\delta\text{-MnO}_2$  on flexible CC, thereby further improving the high-performance AZIBs.

### Data availability

The data supporting this article have been included as part of the ESI.†

### Author contributions

W. J. Z. conceived the project, designed the experiments and wrote the manuscript. Z. B. C. performed theoretical calculation and data curation. C. L. and L. B. Y. performed formal analysis

and writing-review & editing. L. G. Y., L. L. L. and S. S. L. performed data curation. T. M. and D. S. performed funding acquisition, writing – review & editing and supervised this work. Y. X. T. contributed to resources and writing – review & editing. All the authors contributed to the editing and improvement of this manuscript.

## Conflicts of interest

The authors declare no competing financial interests.

## Acknowledgements

This work was financially supported by the National Natural Science Foundation of China (22409065); the project funded by China Postdoctoral Science Foundation (2023M731153); the Guangdong Basic and Applied Basic Research Foundation (2022A1515011906); and the Postdoctoral Fellowship Program of CPSF (GZC20230868).

## References

- 1 Y. Liang and Y. Yao, *Nat. Rev. Mater.*, 2023, **8**, 109–122.
- 2 W. Wen, C. Geng, X. Li, H. Li, J.-M. Wu, H. Kobayashi, T. Sun, Z. Zhang and D. Chao, *Adv. Mater.*, 2024, **36**, 2312343.
- 3 J. Hao, S. Zhang, H. Wu, L. Yuan, K. Davey and S.-Z. Qiao, *Chem. Soc. Rev.*, 2024, **53**, 4312–4332.
- 4 Y. Zeng, D. Luan and X. W. Lou, *Chem*, 2023, **9**, 1118–1146.
- 5 J. Hao, L. Yuan, C. Ye, D. Chao, K. Davey, Z. Guo and S.-Z. Qiao, *Angew. Chem., Int. Ed.*, 2021, **60**, 7366–7375.
- 6 J. Wang, L. Szabo, D. Madhav, I. Ferreira and V. Vandeginste, *Energy Storage Mater.*, 2023, **63**, 103015.
- 7 A. Zhang, R. Zhao, Y. Wang, J. Yue, J. Yang, X. Wang, C. Wu and Y. Bai, *Angew. Chem., Int. Ed.*, 2023, **62**, e202313163.
- 8 Y.-f. Cui, Z.-b. Zhuang, Z.-l. Xie, R.-f. Cao, Q. Hao, N. Zhang, W.-q. Liu, Y.-h. Zhu and G. Huang, *ACS Nano*, 2022, **16**, 20730–20738.
- 9 N. Zhang, F. Cheng, Y. Liu, Q. Zhao, K. Lei, C. Chen, X. Liu and J. Chen, *J. Am. Chem. Soc.*, 2016, **138**, 12894–12901.
- 10 Y. Liu, K. Wang, X. Yang, J. Liu, X.-X. Liu and X. Sun, *ACS Nano*, 2023, **17**, 14792–14799.
- 11 Q. Zhang, J. Zhao, X. Chen, R. Yang, T. Ying, C. Cheng, B. Liu, J. Fan, S. Li and Z. Zeng, *Adv. Funct. Mater.*, 2024, **34**, 2306652.
- 12 W. Li and D. Wang, *Adv. Mater.*, 2023, 2304983.
- 13 H. Cheng, J. Li, T. Meng and D. Shu, *Small*, 2024, **20**, 2308804.
- 14 Y. Zuo, T. Meng, H. Tian, L. Ling, H. Zhang, H. Zhang, X. Sun and S. Cai, *ACS Nano*, 2023, **17**, 5600–5608.
- 15 Y. Wang, Y. Zhang, G. Gao, Y. Fan, R. Wang, J. Feng, L. Yang, A. Meng, J. Zhao and Z. Li, *Nano-Micro Lett.*, 2023, **15**, 219.
- 16 Y. Wang, L. Liu, Y. Wang, J. Qu, Y. Chen and J. Song, *ACS Nano*, 2023, **17**, 21761–21770.
- 17 R. Manjunatha, J. Yuan, L. Hongwei, S.-Q. Deng, E. R. Ezeigwe, Y. Zuo, L. Dong, A. Li, W. Yan, F. Zhang and J. Zhang, *Carbon Energy*, 2022, **4**, 762–775.
- 18 X. Li, F. Chen, B. Zhao, S. Zhang, X. Zheng, Y. Wang, X. Jin, C. Dai, J. Wang, J. Xie, Z. Zhang and Y. Zhao, *Nano-Micro Lett.*, 2023, **15**, 32.
- 19 A. Chowdhury, S. Kumari, A. A. Khan and S. Hussain, *J. Hazard. Mater.*, 2020, **385**, 121602.
- 20 R. Li, O. F. Isowamwen, K. C. Ross, T. M. Holsen and S. M. Thagard, *Environ. Sci. Technol.*, 2023, **57**, 12901–12910.
- 21 C.-W. Lee, S.-B. Yoon, S.-M. Bak, J. Han, K. C. Roh and K.-B. Kim, *J. Mater. Chem. A*, 2014, **2**, 3641–3647.
- 22 Y. Wang, M. Huang, H. Yu, J. Cui, J. Gao, Z. Lou, X. Feng, W. Shan and Y. Xiong, *J. Hazard. Mater.*, 2023, **455**, 131611.
- 23 Y. Deng, H. Wang, M. Fan, B. Zhan, L.-J. Zuo, C. Chen and L. Yan, *J. Am. Chem. Soc.*, 2023, **145**, 20109–20120.
- 24 Z. Li, Y. Li, D. Wang, L. Yuan, X. Liu, C. Pan and X. Zhang, *Chem. Eng. J.*, 2022, **435**, 134968.
- 25 J. Lu, Y.-X. Chang, N.-N. Zhang, Y. Wei, A.-J. Li, J. Tai, Y. Xue, Z.-Y. Wang, Y. Yang, L. Zhao, Z.-Y. Lu and K. Liu, *ACS Nano*, 2017, **11**, 3463–3475.
- 26 T. Meng, B. Li, L. Hu, H. Yang, W. Fan, S. Zhang, P. Liu, M. Li, F. L. Gu and Y. Tong, *Small Methods*, 2019, **3**, 1900185.
- 27 J. Wang, W. Guo, Z. Liu and Q. Zhang, *Adv. Energy Mater.*, 2023, **13**, 2300224.
- 28 C. Zuo, F. Xiong, J. Wang, Y. An, L. Zhang and Q. An, *Adv. Funct. Mater.*, 2022, **32**, 2202975.
- 29 H. Yao, H. Yu, Y. Zheng, N. W. Li, S. Li, D. Luan, X. W. Lou and L. Yu, *Angew. Chem., Int. Ed.*, 2023, **62**, e202315257.
- 30 J. Ling, A. Gao, Y. Huang, F. Yi, Q. Li, G. Wang, Y. Liu and D. Shu, *Chem. Eng. J.*, 2023, **452**, 139661.
- 31 R.-J. Luo, X.-L. Li, J.-Y. Ding, J. Bao, C. Ma, C.-Y. Du, X.-Y. Cai, X.-J. Wu and Y.-N. Zhou, *Energy Storage Mater.*, 2022, **47**, 408–414.
- 32 B. Ouyang, T. Chen, X. Liu, M. Zhang, P. Liu, P. Li, W. Liu and K. Liu, *Chem. Eng. J.*, 2023, **458**, 141384.
- 33 Q. Li, A. Gao, T. Meng, F. Yi, J. Hao, J. Ling and D. Shu, *J. Power Sources*, 2023, **560**, 232705.
- 34 J. Yu, T. Zeng, H. Wang, H. Zhang, Y. Sun, L. Chen, S. Song, L. Li and H. Shi, *Chem. Eng. J.*, 2020, **394**, 124458.
- 35 A. Zhang, R. Gao, L. Hu, X. Zang, R. Yang, S. Wang, S. Yao, Z. Yang, H. Hao and Y.-M. Yan, *Chem. Eng. J.*, 2021, **417**, 129186.
- 36 F. Chen, M. Zhang, L. Ma, J. Ren, P. Ma, B. Li, N. Wu, Z. Song and L. Huang, *Sci. Total Environ.*, 2020, **730**, 138930.
- 37 Z. Cui, F. Yi, T. Meng, A. Gao, J. Hao, Y. Wang, S. Li, J. Huang and D. Shu, *Sustainable Mater. Technol.*, 2023, **37**, e00678.
- 38 X. Zheng, G. Zhang, Z. Yao, Y. Zheng, L. Shen, F. Liu, Y. Cao, S. Liang, Y. Xiao and L. Jiang, *J. Hazard. Mater.*, 2021, **411**, 125180.
- 39 G. Wang, Y. Wang, B. Guan, J. Liu, Y. Zhang, X. Shi, C. Tang, G. Li, Y. Li, X. Wang and L. Li, *Small*, 2021, **17**, 2104557.
- 40 Y. Zhao, S. Zhang, Y. Zhang, J. Liang, L. Ren, H. J. Fan, W. Liu and X. Sun, *Energy Environ. Sci.*, 2024, **17**, 1279–1290.
- 41 C. Lin, J.-L. Li, X. Li, S. Yang, W. Luo, Y. Zhang, S.-H. Kim, D.-H. Kim, S. S. Shinde, Y.-F. Li, Z.-P. Liu, Z. Jiang and J.-H. Lee, *Nat. Catal.*, 2021, **4**, 1012–1023.
- 42 B. Ravel and M. Newville, *J. Synchrotron Radiat.*, 2005, **12**, 537–541.



- 43 D. Chao, C. Ye, F. Xie, W. Zhou, Q. Zhang, Q. Gu, K. Davey, L. Gu and S.-Z. Qiao, *Adv. Mater.*, 2020, **32**, 2001894.
- 44 W. Guo, C. Dun, F. Yang, C. Zhan, J. J. Urban, J. Guo and Q. Zhang, *ACS Nano*, 2023, **17**, 25357–25367.
- 45 J. Hao, B. Li, X. Li, X. Zeng, S. Zhang, F. Yang, S. Liu, D. Li, C. Wu and Z. Guo, *Adv. Mater.*, 2020, **32**, 2003021.
- 46 Q. Chen, X. Lou, Y. Yuan, K. You, C. Li, C. Jiang, Y. Zeng, S. Zhou, J. Zhang, G. Hou, J. Lu and Y. Tang, *Adv. Mater.*, 2023, **35**, 2306294.
- 47 J. Zhang, W. Li, J. Wang, X. Pu, G. Zhang, S. Wang, N. Wang and X. Li, *Angew. Chem., Int. Ed.*, 2023, **62**, e202215654.
- 48 K. Wang, H. Li, Z. Xu, Y. Liu, M. Ge, H. Wang, H. Zhang, Y. Lu, J. Liu, Y. Zhang, Y. Tang and S. Chen, *Adv. Energy Mater.*, 2024, **14**, 2304110.
- 49 Y. Zhao, R. Zhou, Z. Song, X. Zhang, T. Zhang, A. Zhou, F. Wu, R. Chen and L. Li, *Angew. Chem., Int. Ed.*, 2022, **134**, e202212231.
- 50 S. Cui, D. Zhang and Y. Gan, *Adv. Energy Mater.*, 2024, **14**, 2302655.
- 51 L. Dai, Y. Wang, L. Sun, Y. Ding, Y. Yao, L. Yao, N. E. Drewett, W. Zhang, J. Tang and W. Zheng, *Adv. Sci.*, 2021, **8**, 2004995.
- 52 J. Zhang, W. Li, J. Wang, X. Pu, G. Zhang, S. Wang, N. Wang and X. Li, *Angew. Chem., Int. Ed.*, 2023, **135**, e202215654.
- 53 F. Jing, Y. Liu, Y. Shang, C. Lv, L. Xu, J. Pei, J. Liu, G. Chen and C. Yan, *Energy Storage Mater.*, 2022, **49**, 164–171.
- 54 S. Cui, D. Zhang and Y. Gan, *Adv. Energy Mater.*, 2024, **14**, 2302655.
- 55 T. Meng, B. Li, C. Liu, Q. Wang, D. Shu, S. Ou, M. S. Balogun, H. Su and Y. Tong, *Energy Storage Mater.*, 2022, **46**, 344–351.
- 56 X. Zhou, S. Chen, Y. Zhang, B. Yu, Y. Chen, Y. Liu, S. Li, L. Liu, H. Jin, J. Deng and Q. Tan, *Small Struct.*, 2024, **5**, 2400057.
- 57 Q. Wang, H. Yang, T. Meng, J. Yang, B. Huang, F. L. Gu, S. Zhang, C. Meng and Y. Tong, *Energy Storage Mater.*, 2021, **36**, 365–375.
- 58 S. Yao, S. Wang, R. Liu, X. Liu, Z. Fu, D. Wang, H. Hao, Z. Yang and Y.-M. Yan, *Nano Energy*, 2022, **99**, 107391.
- 59 D. Chao, C. Ye, F. Xie, W. Zhou, Q. Zhang, Q. Gu, K. Davey, L. Gu and S. Z. Qiao, *Adv. Mater.*, 2020, **32**, 2001894.
- 60 S. Jiao, X. Fu and H. Huang, *Adv. Funct. Mater.*, 2022, **32**, 2107651.
- 61 D. Ma, Z. Zhao, Y. Wang, X. Yang, M. Yang, Y. Chen, J. Zhu, H. Mi and P. Zhang, *Adv. Mater.*, 2024, **36**, 2310336.
- 62 F. Bu, Z. Sun, W. Zhou, Y. Zhang, Y. Chen, B. Ma, X. Liu, P. Liang, C. Zhong, R. Zhao, H. Li, L. Wang, T. Zhang, B. Wang, Z. Zhao, J. Zhang, W. Li, Y. S. Ibrahim, Y. Hassan, A. Elzatahry, D. Chao and D. Zhao, *J. Am. Chem. Soc.*, 2023, **145**, 24284–24293.
- 63 Z. Sun, F. Bu, Y. Zhang, W. Zhou, X. Li, X. Liu, H. Jin, S. Ding, T. Zhang, L. Wang, H. Li, W. Li, C. Zhang, D. Zhao, Y. Wang and D. Chao, *Angew. Chem., Int. Ed.*, 2024, **63**, e202402987.